



# Photoelectrocatalytic degradation of Rhodamine B by spray deposited $\text{Bi}_2\text{WO}_6$ photoelectrode under solar radiation

R.S. Pedaneekar<sup>a</sup>, S.B. Madake<sup>a</sup>, N.A. Narewadikar<sup>a</sup>, S.V. Mohite<sup>b</sup>, A.R. Patil<sup>a</sup>, S.M. Kumbhar<sup>a</sup>, K.Y. Rajpure<sup>a,\*</sup>

<sup>a</sup> Electrochemical Materials Laboratory, Department of Physics, Shivaji University, Kolhapur 416004, India

<sup>b</sup> Research Institute of Basic Sciences, Incheon National University, Incheon 22012, South Korea

## ARTICLE INFO

### Keywords:

$\text{Bi}_2\text{WO}_6$  photoelectrode  
Spray pyrolysis  
Rietveld refinement  
Photoelectrocatalysis  
Rhodamine B (RhB)

## ABSTRACT

In this work, visible region active  $\text{Bi}_2\text{WO}_6$  thin films with variable thickness are successfully deposited by simple and effective spray pyrolysis technique. The structural, optical, morphological and photoelectrochemical properties of synthesized thin films were studied. Rietveld refinement of the structural data tested purity and degree of crystallinity of  $\text{Bi}_2\text{WO}_6$  thin films synthesized with variable solution quantity. Optical study revealed visible light absorption of films and small variation in band gap energy. A thin film deposited with 70 ml spraying solution quantity exhibit higher photocurrent density ( $460 \text{ mA/cm}^2$ ) and same film with large area ( $10 \times 10 \text{ cm}^2$ ) was used for photocatalytic and photoelectrocatalytic degradation of Rhodamine B (RhB) dye under solar radiation. The photoelectrocatalytic removal of RhB exhibit higher degradation efficiency (94%) as compared to photocatalytic process (23%). This study can trigger potential application of  $\text{Bi}_2\text{WO}_6$  photoelectrode in solar energy conversion, wastewater treatment and energy production.

## 1. Introduction

Nowadays water pollution is one of the serious threat in front of the society. The various dyes, organic species and wastage released from rural, urban and industrial activity leaked into the streamline water bodies pose to water pollution [1]. Worldwide, the millions of deaths are related to the water borne diseases. The direct discharge of hazardous contaminants into the surface water resources like rivers, ocean lakes etc. is a serious environmental issue. Therefore, it is crucial to degrade these pollutants by using the appropriate method [2]. Several techniques have been employed for environmental remediation including advanced oxidation processes (AOPs), adsorption, photo-Fenton systems, ultrasound, reverse osmosis, chlorination, ozonation, photolysis ( $\text{UV}/\text{H}_2\text{O}_2$ ), membrane process, coagulation and biological methods. Among these, AOPs like heterogeneous photocatalysis are emerging as a leading technology for degradation of various organic pollutants [3–5]. Finegold and Cude first time introduced the decomposition of water into  $\text{H}_2$  and  $\text{O}_2$  by semiconductor catalysts under solar irradiation. This technique has great potential to convert solar energy into chemical energy for the mineralization of organic pollutants [6,7]. The AOPs involves the generation of anions and highly oxidizing hydroxyl radical to

degrade the toxic pollutants into harmless product. It carries enormous potential to degrade various pollutants and waste water treatment. The photocatalysis technique is a promising, cost effective, efficient, and green approach for environmental remediation. It has wide range of applications such as waste water treatment, self-cleaning applications, artificial photosynthesis, cancer treatment,  $\text{H}_2$  generation, structural applications, photochemical devices, selective oxidation and reduction, dye sensitized solar cells and removal of toxic gases from air [8–11].

Various metal oxides and metal sulfides such as  $\text{TiO}_2$ ,  $\text{ZnO}$ ,  $\text{WO}_3$ ,  $\text{Bi}_2\text{O}_3$ ,  $\text{Cu}_2\text{O}$ ,  $\text{CuO}$ ,  $\text{CeO}_2$ ,  $\text{Fe}_2\text{O}_3$ ,  $\text{BiVO}_4$ ,  $\text{Bi}_2\text{WO}_6$ ,  $\text{CdS}$ ,  $\text{ZnS}$ , etc. are widely studied for photocatalytic applications [12]. Among these the photocatalytic performance of  $\text{TiO}_2$  and  $\text{ZnO}$  is extensively studied because of their remarkable properties such as excellent chemical stability, non-toxicity, low cost and higher oxidation stability. However, they are still struggling with the efficiency as they absorb only UV radiation (only 4% of solar spectrum) due to their wide band gap energies [13]. Therefore, recently a lot of effort is being made on the development of visible active photocatalyst to cover larger portion (44%) of the solar spectrum [14]. Bismuth tungstate ( $\text{Bi}_2\text{WO}_6$ ) is a visible region active significant metal oxide semiconductor photocatalyst and has emerged as a promising candidate for waste water treatment. It is a

\* Corresponding author.

E-mail address: [rajpureky@gmail.com](mailto:rajpureky@gmail.com) (K.Y. Rajpure).

<https://doi.org/10.1016/j.matresbull.2021.111639>

Received 30 June 2021; Received in revised form 8 November 2021; Accepted 9 November 2021

Available online 13 November 2021

0025-5408/© 2021 Elsevier Ltd. All rights reserved.

n-type direct band gap semiconductor which exhibits remarkable properties like ferroelectricity, dielectric susceptibility, better chemical and thermal stabilities, high Curie temperature and piezoelectricity.  $\text{Bi}_2\text{WO}_6$  is a simple member of Aurivillius family and consists of Layers of  $(\text{Bi}_2\text{O}_2)^{2+}$  and perovskite  $(\text{WO}_4)^{2-}$  [15,16]. The  $\text{Bi}_2\text{WO}_6$  has potential to degrade various pollutants such as methylene blue [17], RhB [18], rhodamine 6 G [19], phenol [20], etc.  $\text{Bi}_2\text{WO}_6$  powder was used in mobile catalysis. There is difficulty in recollection of powder photocatalyst after degradation reaction and causes aggregation due to loading of higher photocatalyst. Therefore, the use of thin film photocatalyst in mobile catalysis is a cost effective alternate and stable route for photocatalytic applications [8,21]. Several techniques have been employed for  $\text{Bi}_2\text{WO}_6$  thin film deposition such as dip coating [22], Aerosol-Assisted Chemical Vapor Deposition (AACVD) [23], spray pyrolysis [18], layer-by-layer technique [24], reactive magnetron sputtering [25], spin coating [26], direct chemical deposition [27], etc. Among these, chemical spray pyrolysis has been attractive and novel due to its advantages in large area oxide film formation. Alfaifi et al. reported the effect of annealing temperature on the photodegradation of RhB by spray deposited  $\text{Bi}_2\text{WO}_6$  thin film and found that degradation efficiency increases with annealing temperature [18]. However, this film showed comparatively lower photoelectrochemical performance.

In the present work, sprayed deposited large area ( $10 \times 10\text{cm}^2$ )  $\text{Bi}_2\text{WO}_6$  photoelectrode are employed in degradation reactor and studied the photoelectrocatalytic and photocatalytic degradation performance for RhB dye degradation under solar radiation. The comparative studied found that the photoelectrocatalytic degradation process are more effective than that of photocatalytic process and has high degradation efficiency. The obtained results showed that  $\text{Bi}_2\text{WO}_6$  thin films are helpful for RhB degradation using sunlight.

## 2. Experimental details

### 2.1. Material and methods

All the commercially available chemicals of analytical grade were used for synthesis without further purification. Bismuth nitrate pentahydrate [ $\text{Bi}(\text{NO}_3)_3 \cdot 5\text{H}_2\text{O}$ ] AR (Thomas Baker, Mumbai, India) and tungsten metal powder (Sigma-Aldrich chemicals, Bangalore, India) were used as precursors. Hydrogen peroxide (30% W/V Thomas Baker, Mumbai, India), double distilled water and  $\text{HNO}_3$  (Thomas Baker,

Mumbai, India) were used as solvents for the preparation of precursor solution. Sodalime and Fluorine-doped tin oxide (FTO,  $R \sim (10-15) \Omega/\text{cm}^2$ ) coated glass substrates were used to deposit  $\text{Bi}_2\text{WO}_6$  thin films.

### 2.2. Thin film preparation

The chemical spray pyrolysis method was adopted for the synthesis of  $\text{Bi}_2\text{WO}_6$  thin films onto the preheated sodalime and FTO coated glass substrate. The appropriate amount of  $\text{Bi}(\text{NO}_3)_3 \cdot 5\text{H}_2\text{O}$  were dissolved in diluted  $\text{HNO}_3$  solution to get clear solution. 0.5 M stock solution of peroxotungstic acid (PTA) was prepared by dissolving 2.77 g of tungsten powder in  $\text{H}_2\text{O}_2$ . The strong exothermic reaction between  $\text{H}_2\text{O}_2$  and tungsten powder was avoided by keeping  $\text{H}_2\text{O}_2$  containing beaker in an ice bath over the period of 30 min. Afterwards, resulting milky solution was kept on constant stirring for 48 h for complete dissolution of tungsten powder. The transparent PTA solution was obtained by the filtration of stirred solution and preserved under dark environment. The tungsten precursor solution for deposition was obtained by dissolving appropriate amount of PTA stock solution into double distilled water. The final precursors solution was obtained by appropriate composition of these two solutions contains Bi and W ions. The deposition was carried on both preheated sodalime and FTO coated glass substrates. The volume of the spraying solution was varied from 50 to 80 ml at the interval of 10 ml and other preparative parameters such as substrate temperature ( $325^\circ\text{C}$ ), flow rate (4 ml/min), nozzle to substrate distance (31 cm), etc. were kept constant for all the experiments. The optimum volume of spraying solution was confirmed by photoelectrochemical study and large area photoelectrode ( $10 \times 10\text{cm}^2$ ) for degradation experiment was synthesized with optimized deposition parameters. The set of samples deposited with solution quantity 50 ml, 60 ml, 70 ml and 80 ml were labeled, respectively as BWO1, BWO2, BWO3 and BWO4. The main purpose of changing the spraying solution volume was to monitor the film thickness. The aim been to obtain optimum thickness for achieving higher catalytic degradation efficiency.

### 2.3. Material characterization

The photoelectrochemical response of the thin films were recorded with three electrode configuration by adopting linear sweep voltammetry (LSV) technique. An aqueous solution of 1 M NaOH was used as an electrolyte. The  $\text{Bi}_2\text{WO}_6$  film deposited on FTO glass acts as a working electrode, Platinum wire acts as a counter electrode, 500 W tungsten filament as light source and standard calomel electrode (SCE) was used as a reference electrode. The distance between working and counter electrodes was kept 0.5 cm throughout the experiment. The working electrode was illuminated from backside with light source and contact area at working-electrolyte interface was  $1\text{cm}^2$ .

The structural data were recorded by Bruker X-ray diffractometer Model D2: phaser with CuK-alpha radiation of wavelength  $1.5418\text{ \AA}$ . The surface morphology of films was captured by Tescan, Mira3 field emission scanning electron microscope (FESEM). Elemental identification and their respective compositions were determined by using Energy Dispersive X-ray analysis (EDX). The Raman spectrum was recorded by Renishaw inVia Raman microscope and surface topography was studied by Park, NX10 atomic force microscope (AFM). UV-Vis spectrophotometer (UV1800, Shimadzu) was used to study optical properties.

### 2.4. Degradation of RhB

RhB dye (30 mg/L) was used as model organic pollutant for the degradation experiment. For both photocatalytic and photoelectrocatalytic degradation processes, the single cell PEC reactor was used in which large area ( $10 \times 10\text{cm}^2$ ) deposited  $\text{Bi}_2\text{WO}_6/\text{FTO}$  film acted as working electrode and stainless-steel body of cell as a counter electrode. These electrodes were separated by distance of 0.1 cm

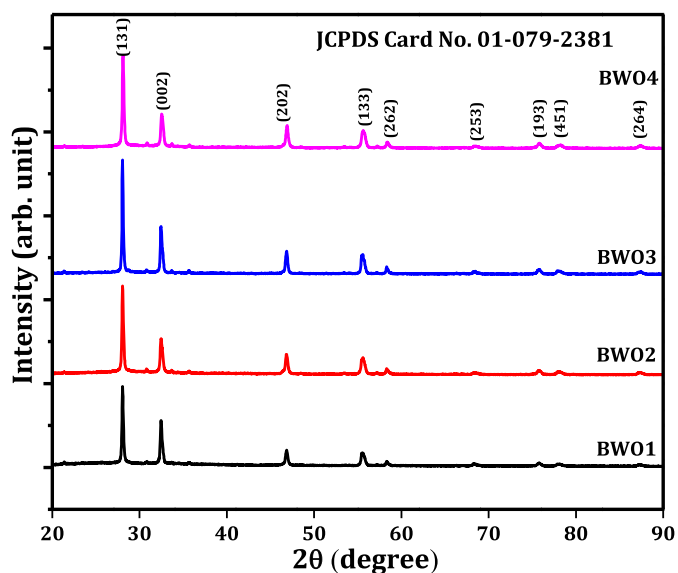


Fig. 1. X-ray diffraction pattern of  $\text{Bi}_2\text{WO}_6$  thin films with variation in spraying quantity.

**Table 1**

a: Atomic positions of BWO3 film after the Rietveld refinement b: Lattice parameter, density, direct cell volume and Bragg R-factor of Bi<sub>2</sub>WO<sub>6</sub> thin films by Rietveld refinement method.

Atom	x	y	z	B	Occupancy					
Bi1	0.52055	0.42238	0.97608	0.43584	1					
Bi2	0.4824	0.07712	0.97956	0.59533	1					
W	0.00706	0.24948	0.0000	0.1587	1					
O1	0.08361	0.17775	0.51068	0.85194	1					
O2	0.41419	0.8	0.60301	0.68692	1					
O3	0.93894	0.49484	0.23243	0.39715	1					
O4	0.48632	0.12894	0.369	0.78562	1					
O5	0.07145	0.32619	0.51212	0.95696	1					
O6	0.45506	0.35091	0.52417	0.68929	1					
Sample	Lattice parameter			Density (g/cm <sup>3</sup> )	Cell Volume (Å <sup>3</sup> )	R <sub>wp</sub> (%)	R <sub>B</sub> (%)	R <sub>exp</sub> (%)	χ <sup>2</sup>	
	a (Å)	b (Å)	c (Å)							
BWO1	5.4692	16.3161	5.4747	9.488	488.537	28.3	11.06	17.6	2.569	
BWO2	5.4388	16.3793	5.4714	9.509	487.415	26.4	8.144	15.2	3.005	
BWO3	5.4604	16.2986	5.4712	9.519	486.915	24.8	8.55	14.7	2.841	
BWO4	5.4615	16.3253	5.4719	9.501	487.875	21.2	5.44	13.6	2.421	
CIF file No. 9011799	5.437	16.430	5.458	9.505	487.563	5.94	-	5.17	1.32	

through a Teflon made gasket which functions to support circulation of organic pollutant solution in between inlet and outlet of the cell. The total geometrical area of the Bi<sub>2</sub>WO<sub>6</sub>/FTO photoelectrode in contact with the pollutant was ~ 64 cm<sup>2</sup>. The re-circulation of electrolyte was carried out by using a Gilson MINIPLUS peristaltic pump, made in France with constant flow rate in order to bring maximum number of

impurities in contact with Bi<sub>2</sub>WO<sub>6</sub> thin film photocatalyst. The total volume of single cell reactor was 6 ml and supported on a z-shaped stand. The backside of BWO3 photoanode was illuminated by solar light and potential was applied to the contacts made at corners of the BWO3/FTO photoelectrode. During the degradation reaction, 1 ml sample from reaction mixture was collected after certain time interval. The

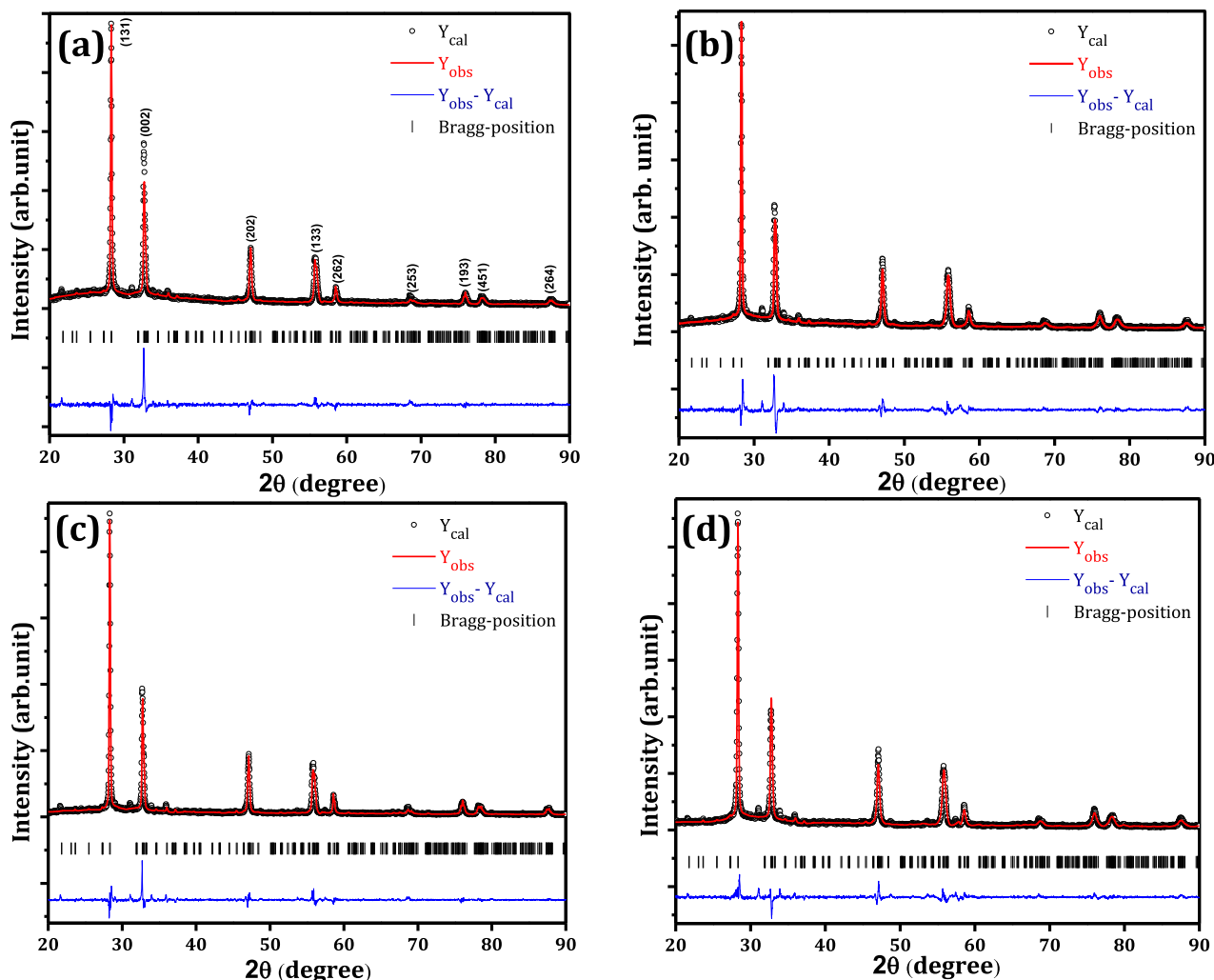


Fig. 2. Rietveld refinement plots of (a) BWO1 (b) BWO2 (c) BWO3 and (d) BWO4 films.

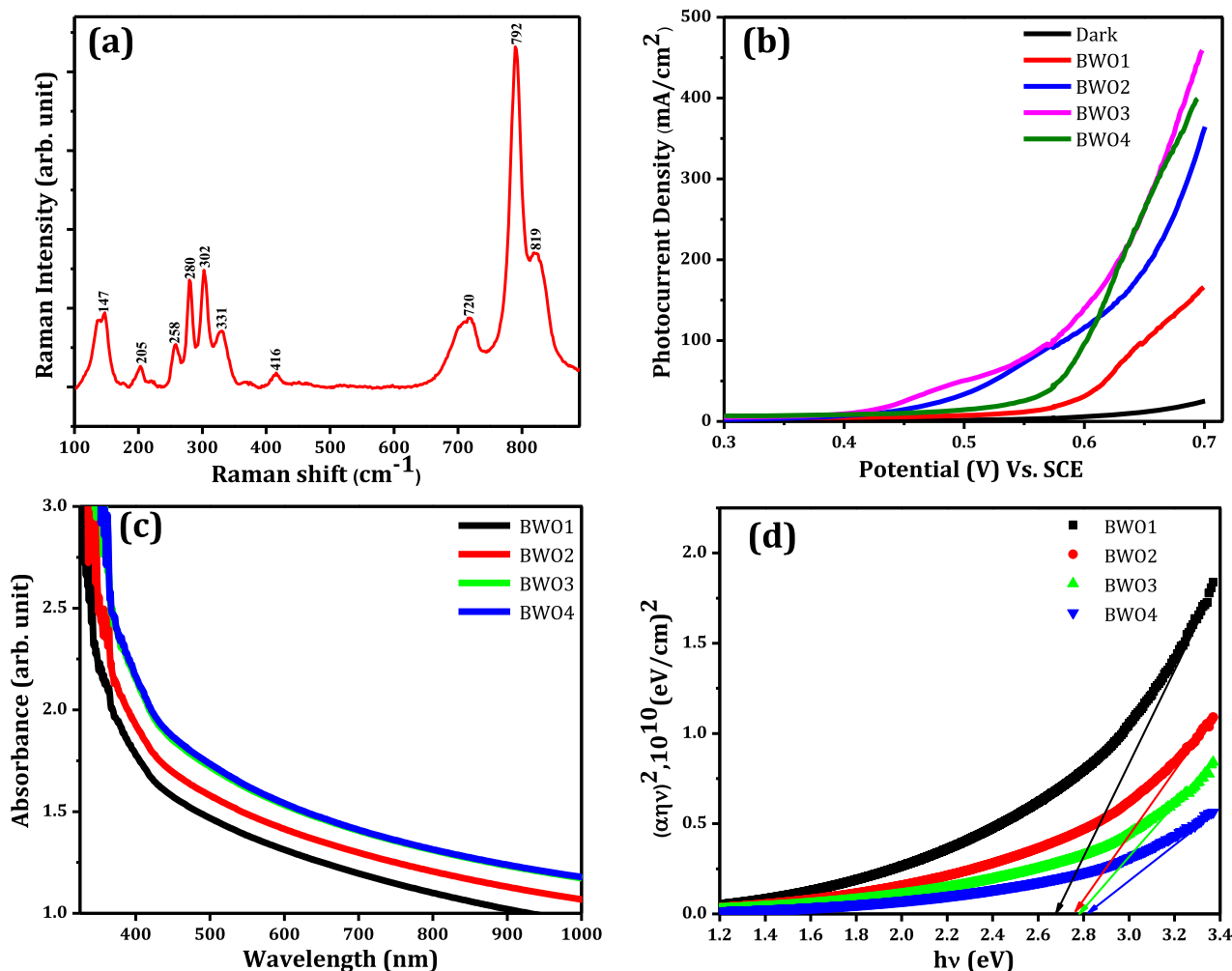


Fig. 3. (a) Raman spectrum of synthesized BWO3 sample, (b) Photoelectrochemical performance of  $\text{Bi}_2\text{WO}_6|1\text{ M NaOH}| \text{Pt}$  photoelectrochemical cell, (c) Optical absorption spectra and (d) Variation in band gap energy of  $\text{Bi}_2\text{WO}_6$  films with various volume of spraying solution. (For interpretation of the references to color in this figure, the reader is referred to the web version of this article.)

absorbance spectra were recorded by UV-Vis spectrophotometer to determine degradation performance of BWO3 photocatalyst using RhB dye.

### 3. Results and discussion

#### 3.1. Structural analysis

The XRD patterns of spray deposited  $\text{Bi}_2\text{WO}_6$  thin films are shown in Fig. 1. The presence of multiple peaks in XRD patterns are confirmed polycrystalline nature of synthesized films. The diffraction peaks position in XRD patterns are well-matched with standard JCPDS card No. 01-079-2381 and confirms orthorhombic crystal structure with preferred orientation along (131) plane having  $\text{Pca}2_1$  space group. The peak intensity increased upto 70 ml spraying quantity due to increase in crystallinity and afterwards it was found to be decreased as a consequence of formation of powdery and less adherent films [28]. The average crystallite sizes of the films were calculated using well known Debye Scherer formula,  $D = 0.9\lambda / \beta \cos\theta$ , and were found in the range of 40–50 nm. Films with better crystallinity will not have much light scattering thereby improving probability of light absorption at the semiconductor-liquid junction which in turns will lead to improved quantum yield and higher photocurrent. Powdery film would led to light scattering and lower photocurrent.

The Rietveld refinement method by using *Fullprof* software was adopted to analyze crystalline architecture and variation in crystallinity of the films with variable solution quantity. This study confirmed orthorhombic phase of the  $\text{Bi}_2\text{WO}_6$  films with  $\text{Pca}2_1$  space group and absence of any secondary phase. Initially the required background was obtained from powder diffraction profile with the help of automatic background (with threshold 0.05) function in *Fullprof* software. Peak shape function used was Pseudo-Voigt. Initial input parameters for the refinement were adopted from CIF file No. 9011799 reported by Knight [29]. Then the other parameters were fixed and only the following parameters were refined in sequence given: background, lattice parameters, scale factor, overall B-factor, FWHM parameters U, W and atomic positions.

Cycle of refinement used were 20. The  $\chi^2$  factor and the difference plot were monitored during each refinement calculation. The goal was to obtain least  $\chi^2$  and almost flat difference plot, without violating any physical rule. Table 1a represents atomic positions of Bi, W and O obtained after the refinement and 1b lists output parameters such as lattice parameter ( $a$ ,  $b$  and  $c$ ), weight profile factor ( $R_{wp}$ ), profile factor ( $R_p$ ), cell volume, compound density, expected weighted profile factor ( $R_{exp}$ ), Reduced chi-square ( $\chi^2$ ), and Bragg factor ( $R_B$ ). The lattice parameters of all films were found to be similar with lattice parameters that reported in JCPDS file (01-079-2381). Fig. 2 indicates the fitting of experimentally observed data against theoretically calculated data and goodness of

fitting was decided by the nature of ( $Y_{obs} - Y_{cal}$ ) line. Excellent agreement between experiment and calculated data was found as reflected from the values of R-factors. In the Rietveld method following relations are generally used to obtain various output parameters of sample under study after the refinement.

Weighted profile factor:

$$R_{wp} = \left[ \frac{\sum_{i=1}^n W_i |y_{obs,i} - y_{cal,i}|^2}{\sum_{i=1}^n W_i y_{obs,i}^2} \right]^{1/2} \times 100 \quad (1)$$

Expected weighted profile factor:

$$R_{exp} = \left[ \frac{n - p}{\sum_{i=1}^n W_i y_{obs,i}^2} \right]^{1/2} \times 100 \quad (2)$$

Bragg factor:

$$R_B = \left[ \frac{\sum_h |I_{obs,h} - I_{cal,h}|}{\sum_h |I_{obs,h}|} \right] \times 100 \quad (3)$$

Crystallographic  $R_f$  factor:

$$R_F = \left[ \frac{\sum_h |F_{obs,k} - F_{cal,h}|}{\sum_h |F_{obs,h}|} \right] \times 100 \quad (4)$$

$$\text{Reduced chi - square } (\chi^2) = \left( \frac{R_{wp}}{R_{exp}} \right)^2 \quad (5)$$

Where,  $y$ ,  $w$ ,  $n$ ,  $p$ ,  $I$ , and  $F$  are profile intensities, suitable weights taken from experimental error margin, number of observations (data points), number of parameters, integrated intensities, and structure factors, respectively. Subscripts 'obs' and 'cal' represent observed parameters and calculated parameters, respectively. These obtained output parameters support reliability and accuracy of the refinement.

$\text{Bi}_2\text{WO}_6$  is a ternary metal oxide composed of alternating layers of  $(\text{Bi}_2\text{O}_2)^{2+}$  and perovskite  $(\text{WO}_4)^{2-}$  stacks. With apical oxygen  $\text{WO}_6$  octahedrons are linked together and equatorial oxygen connects  $\text{WO}_6$  and more complex  $\text{BiO}_6$  polyhedrons [30]. At room temperature,  $\text{Bi}_2\text{WO}_6$  structure with  $\text{Pca}2_1$  space group exhibits  $2A_{1g} + B_{1g} + 3E_g + 4A_{2u} + B_{2u} + 5E_u$  optic modes. Among these,  $2A_{1g}$ ,  $B_{1g}$  and  $3E_g$  are Raman active modes and the rest are IR active. These modes are associated with several possible vibration such as asymmetric ( $A_{2u}$ ) and symmetric ( $A_{1g}$ ) stretching of  $\text{WO}_6$  (apical oxygen atoms), asymmetric ( $E_u$ ) stretching of  $\text{WO}_6$  (equatorial oxygen atoms), vibrations involving translational motions of  $\text{Bi}^{3+}$  and  $\text{W}^{6+}$  ions ( $A_{2u} + E_u$ ), bending ( $E_g + A_{2u} + B_{2u} + 2E_u$ ) vibrations of  $\text{WO}_6$  and stretching and bending ( $B_{1g} + E_g + A_{2u} + E_u$ ) vibrations of  $(\text{Bi}_2\text{O}_2)^{2+}$  layer.

Fig. 3(a) shows Raman spectrum of the BWO3 thin film. The peak positions are evident to orthorhombic phase of the  $\text{Bi}_2\text{WO}_6$ . The stretching of the W–O bonds are assigned by the bands in the range 600–900  $\text{cm}^{-1}$ . The bands at 205  $\text{cm}^{-1}$ , 258  $\text{cm}^{-1}$ , 280  $\text{cm}^{-1}$ , 302  $\text{cm}^{-1}$  and 331  $\text{cm}^{-1}$  is associated with bending vibrations of  $\text{WO}_6$  and  $(\text{Bi}_2\text{O}_2)^{2+}$  layer. The peak position at 720  $\text{cm}^{-1}$  illustrates the antisymmetric bridging mode associated with the tungstate chain. While, the peaks observed at 792  $\text{cm}^{-1}$  and 819  $\text{cm}^{-1}$  are assigned to asymmetric ( $A_{2u}$ ) and symmetric ( $A_{1g}$ ) stretching modes of the terminal O–W–O groups in the  $\text{WO}_6$  octahedral. [7,19,31]. These obtained results confirm the formation of  $\text{Bi}_2\text{WO}_6$  thin films.

### 3.2. Photoelectrochemical performance

Fig. 3(b) illustrates the photoelectrochemical performance of  $\text{Bi}_2\text{WO}_6$  photoelectrodes. The behavior of photocurrent density against applied potential range within 0–0.7 V was studied by LSV method with scan rate of 10 mV/s. The BWO3 thin film shows higher photocurrent density, it may be due to higher crystallinity and quantum yield. The photocurrent density ( $J_{ph}$ ) found to be increased with applied potential,

**Table 2**

Variation of photocurrent density and band gap energy with spraying solution quantities.

Solution quantity (ml)	Photocurrent density ( $\mu\text{A}/\text{cm}^2$ )	Band gap energy (eV)
50	170	2.68
60	366	2.74
70	460	2.78
80	395	2.82

this might be due to the availability of large effective semiconductor-electrolyte interface [18]. Further, comparatively higher photocurrent density of this film against the applied potential may be attributed to its optimum thickness (750 nm) and well crystalline growth which offered easier route for charge carrier transportation. In this experiment, getting more photocurrent is considered to be signature of more degradation. In the degradation, more is the rate of catalytic oxidation; more are the electrons released. The lower  $J_{ph}$  value at higher solution quantity attributed increase in film thickness which leads to powdery nature of the film and induces scattering of light which results in lower quantum yield. Table 2 indicates photocurrent density of  $\text{Bi}_2\text{WO}_6$  film with variable solution quantity.

### 3.3. Optical study

The optical absorption spectra of  $\text{Bi}_2\text{WO}_6$  films with variable solution quantity is shown in Fig. 3(c). Absorption edge is red shifted with increase in solution quantity. The major visible region absorption of the films is responsible for enhanced photoactivity. The steep shape of absorbance curve indicates absorption is due to band gap transition and not because of impurity transitions [32]. The optical absorption spectra was analyzed by using following relation [33].

$$\alpha h\nu = A(h\nu - E_g)^n \quad (6)$$

where,  $\alpha$  is absorption coefficient,  $A$  is the constants,  $h\nu$  is photon energy,  $E_g$  is band gap energy of the material and  $n$  is the order. Fig. 3(d) depicts the variation of  $(\alpha h\nu)^2$  v/s energy with respect to volume of spraying solution. The characteristics of transition in semiconductor are decided by the value of  $n$ . The transition corresponding to  $n$  values 1/2, 2, 1/3 and 2/3 are direct allowed, indirect allowed, forbidden indirect and forbidden direct optical transition, respectively. The band gap values of all films were calculated by extrapolating linear part of the curve obtained by plotting  $(\alpha h\nu)^2$  against energy  $h\nu$  to zero absorption coefficient ( $\alpha = 0$ ). Table 2 summarizes variation of band gap energy with solution quantity. The difference in band gap energy is due to the difference in crystalline structure of material with respect to change in quantity. In powdery film, the amorphous content could be responsible for increase in band gap energy.

### 3.4. Morphological and compositional study

The FESEM micrographs of  $\text{Bi}_2\text{WO}_6$  films are shown in Fig. 4(a–d) designates random sized interconnected microparticle and porous morphology. The BWO3 film showed comparatively higher porous structure and interconnected network which may enhance photo-generated charge carrier transport. At higher solution quantity, slight agglomeration of particles responsible for reduced PEC performance. The surface topography of sample BWO3 was analyzed by atomic force microscopy (AFM) with non-contact imaging mode. The histogram is recorded over 1  $\mu\text{m} \times 1 \mu\text{m}$  scan area. Fig. 5(b, c) shows both 2D and 3D images and average roughness of the film was found to be < 25 nm.

The surface area is directly linked to the surface roughness, therefore rough morphology observed for BWO3 significantly contributed to photodegradation performance [34]. Energy dispersive X-ray spectra (EDX) of BWO3 film (Fig. 5(a)) shows the peaks regarding the elements O, Bi, and W. It does not have any impurity peaks that reveals absence of

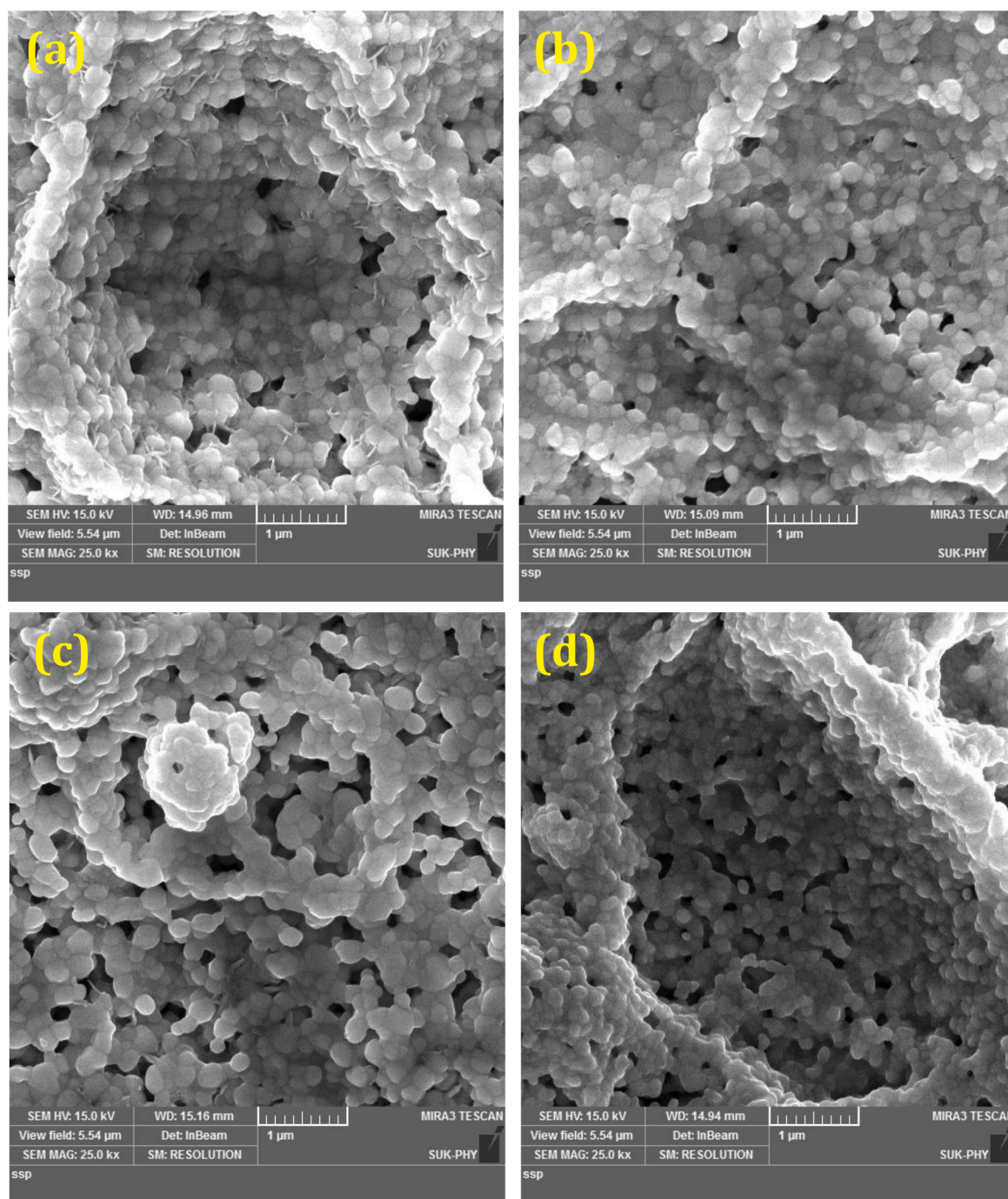


Fig. 4. FE-SEM micrograph of (a) BiWO<sub>6</sub> (b) BiWO<sub>2</sub> (c) BiWO<sub>3</sub> and (d) BiWO<sub>4</sub> film.

foreign elements. The elemental ratios given in Table 3 confirmed the stoichiometry of film material, as the expected and observed elemental proportions are matched.

### 3.5. Charge transfer study

Electrochemical impedance spectroscopy (EIS) was used to examine charge separation characteristic of Bi<sub>2</sub>WO<sub>6</sub> photoelectrode during degradation phenomena. Fig. 6(a) represents Nyquist plot of Bi<sub>2</sub>WO<sub>6</sub>|1MNaOH|Pt cell prepared with different spaying solution quantity under dark, light, and light + bias conditions. The radius of the arc is a rate of reaction which occurs at the electrode surface and is significantly related to separation of photogenerated charge carriers. Under light

illumination, large arc radius revealing poor separation of charges. However, drastic reduction in arc radius was observed after applying bias potential to the electrode. The smaller radius value for BiWO<sub>3</sub>|1M NaOH|Pt cell indicates fast interfacial charge transfer of photoelectron-holes and effective separation of these charge carriers as compare to other cells. The only one arc appeared in the plot suggests both photocatalysis and photoelectrocatalysis are appear to be simple electrode processes [35,36]. This study supports enhanced performance of RhB degradation after applying the external bias potential.

### 3.6. Band edge analysis of Bi<sub>2</sub>WO<sub>6</sub>

In Bi<sub>2</sub>WO<sub>6</sub> photocatalyst, hybridization of Bi 6s and O 2p states

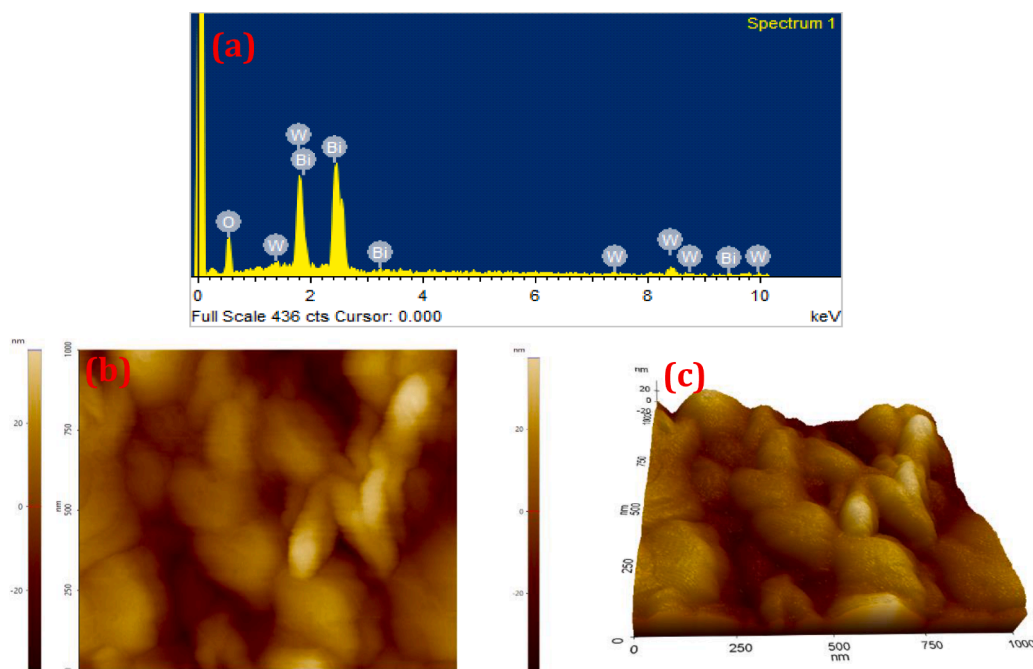


Fig. 5. (a) EDAX spectrum, (b) 2D and (c) 3D AFM images of the BWO3 film.

Table 3  
Elemental ratio of BWO3 film from EDAX analysis.

Elemental ratio	Expected	Observed
W:Bi	0.50	0.55

constitute valance band and W 5d composes conduction band. After light illumination, oxidation and reduction phenomena at catalyst-pollutant interface are mainly depends on band positions of catalyst. Band positions dominates both dissociations of excited charge carriers over surrounding medium and photoexcitation process. The degradation

performance is always dominated by generation rate of reactive oxidation species. Band edge potential of the catalyst decides which reactive species take part in the mineralization of the pollutant. The band position of the semiconductors is related to its electronegativity and it can be calculated by geometric mean of electronegativity of all constituent atoms of the semiconductor [37].

The conduction band minima ( $E_{CB}$ ) and valance band maxima ( $E_{VB}$ ) was calculated by the following Butler and Shinley's relation [38],

$$E_{CB} = \chi(s) - \frac{1}{2}(E_g) - E_0 \tag{7}$$

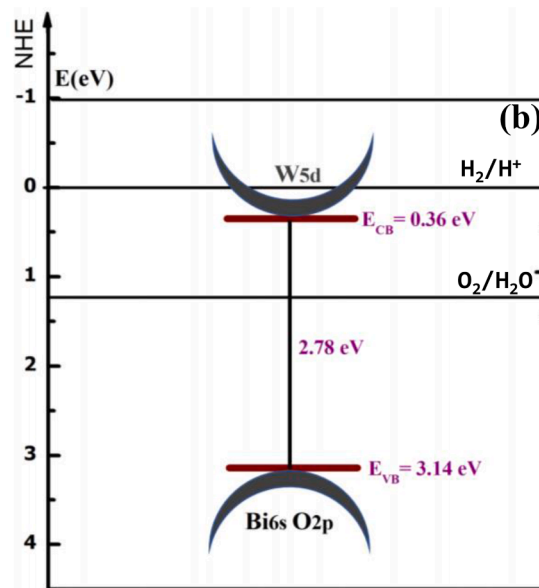
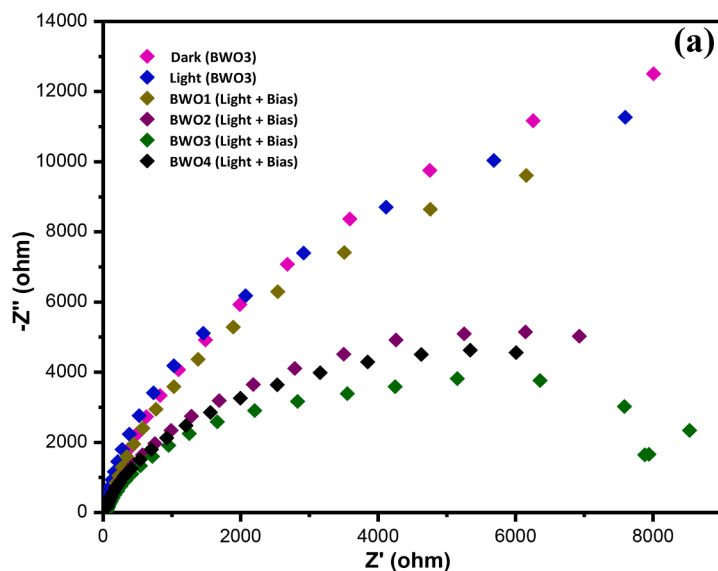


Fig. 6. (a) EIS spectra of  $Bi_2WO_6$  film synthesized with variable solution quantity under dark, light, and light + bias conditions and (b) Band edge positions of BWO3 film against normal hydrogen electrode (NHE).

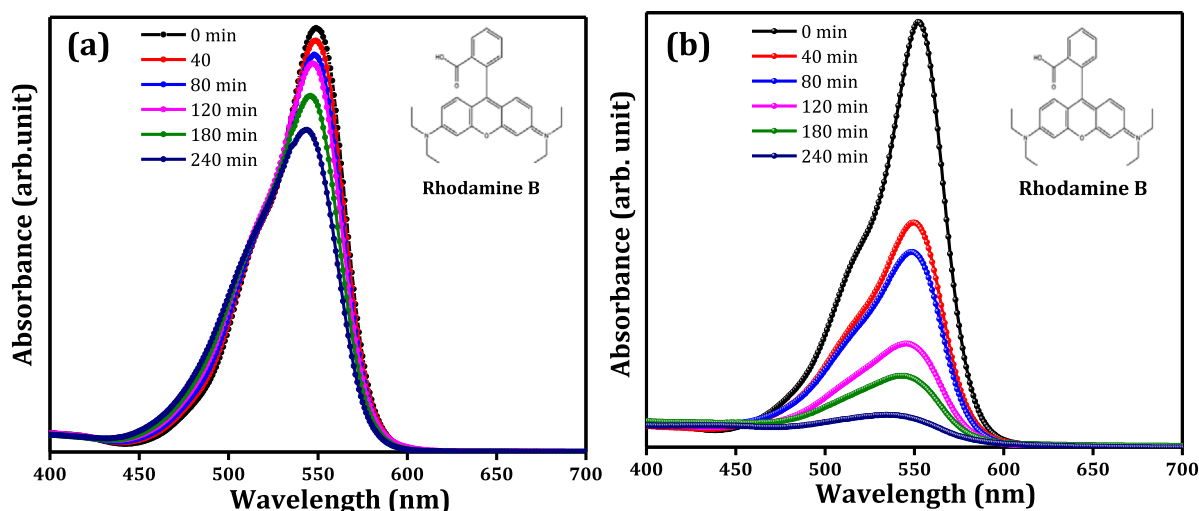


Fig. 7. Degradation of Rhodamine B (RhB) by  $\text{Bi}_2\text{WO}_6$  photocatalyst under solar radiation (a) photocatalysis and (b) photoelectrocatalysis.

$$E_{\text{VB}} = E_{\text{CB}} - E_{\text{g}} \quad (8)$$

Where,  $E_{\text{g}}$  is the band gap energy,  $\chi(\text{s})$  electronegativity of semiconductor, and  $E_0$  is the factor relating the reference electrode redox level to the absolute vacuum scale ( $E_0 = 4.5 \text{ eV}$  for NHE). Based on above equations, Fig. 6(b) represents schematic of band positions of  $\text{Bi}_2\text{WO}_6$  film. More positive potential value of valance band (3.14 eV) signifies higher oxidation potential of  $\text{Bi}_2\text{WO}_6$  catalyst to decompose various organic pollutant. Further, conduction band potential (0.36 eV) is enough to produce superoxide anion ( $\text{O}_2^-$ ) radical in the aqueous solution. The above calculated  $E_{\text{CB}}$  and  $E_{\text{VB}}$  values are found similar to earlier reported values [39].

### 3.7. Photoelectrocatalytic activity of RhB

The detailed investigation of photoelectrocatalytic and photocatalytic degradation of RhB dye as a model organic species for  $\text{Bi}_2\text{WO}_6$  photoelectrode were carried out under solar light illumination. The experiment was performed during sunny weather between 11am and 3pm at Kolhapur, India ( $16.6780^\circ \text{ N}$ ,  $74.2555^\circ \text{ E}$ ). The extinction spectra were recorded during degradation experiment in wavelength range 300 to 700 nm over specific reaction time interval as shown in Fig. 7(a, b). It

indicates decrease in concentration of organic species with the reaction time. The degradation efficiencies were calculated by using the following relation [40].

$$\% \text{ degradation} = \left( \frac{C_0 - C_t}{C_0} \right) \times 100 \quad (9)$$

Here,  $C_0$  is the initial concentration,  $C_t$  is concentration at different time interval and  $t$  is the reaction time. As shown in Fig. 7(a), decrement in height of absorbance peak at 555 nm wavelength with increase in reaction time was observed for photocatalytic reaction and yields degradation efficiency of about 28% within 240 min under solar radiation. This lower efficiency was the consequences of aggressive recombination of photogenerated electrons and holes. The poor interaction of excited electrons in the conduction band with electron acceptors to produce reactive species. As a result, accumulation of electron at the bottom of conduction band may enhanced the recombination rate of charge carriers further. Therefore, separation of charge carriers is an effective route to improve the photocatalytic degradation of RhB [20].

The potential of 0.7 V was applied across the photoanode and cathode to support charge carrier transfer through the external circuit in the single cell reactor. As shown in Fig. 7(b), the extinction spectra of RhB reveals the faster photoelectrocatalytic degradation over 240 min

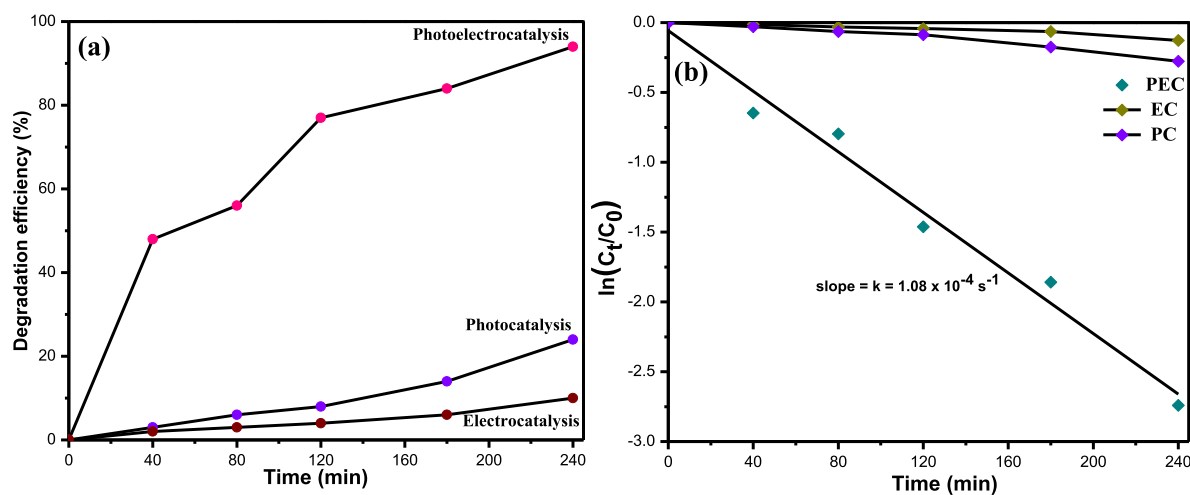


Fig. 8. (a) Photocatalytic, electrocatalytic, and photoelectrocatalytic degradation efficiency of  $\text{Bi}_2\text{WO}_6$  over RhB under solar radiation and (b) Kinetics of degradation reaction of RhB under solar radiation.

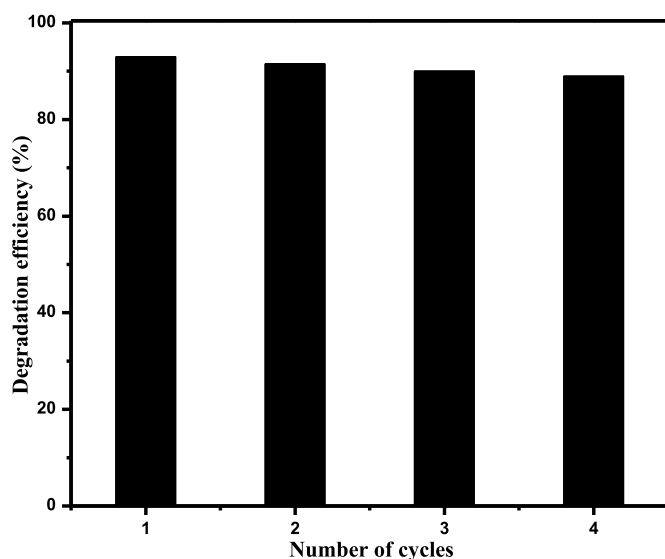


Fig. 9. Stability and recyclability of  $\text{Bi}_2\text{WO}_6$  photoelectrode towards RhB degradation under solar radiation.

under solar radiation. The application of external electrical bias potential enhances degradation efficiency to 94% which is 3 fold higher than photocatalytic performance due to enhanced charge separation characteristic of  $\text{Bi}_2\text{WO}_6$  photoelectrode. Fig. 8(a) indicates comparative study of efficiencies of photocatalytic (PC), electrocatalytic (EC), and photoelectrocatalytic (PEC) degradation of RhB. The electrocatalytic process at bias potential 0.7 V yielded no appreciable degradation of RhB. Further, the synergetic effect of photocatalytic and electrochemical process in PEC treatment is attributed to higher PEC degradation efficiency than the sum of PC and EC efficiencies.

As per the report published earlier, formation of gradient at the  $\text{Bi}_2\text{WO}_6$  surface effectively separates photogenerated charge carriers [35]. After incidence of photons ( $h\nu_{\text{ph}} \geq 2.78$  eV) on the  $\text{Bi}_2\text{WO}_6$  photoelectrode, electrons from valance band (VB) get excited to conduction band leaving behind holes in the VB. The electrons travel through the external circuit to counter electrode assists the formation of highly reactive superoxide anion radicals ( $\text{O}_2^-$ ) which takes part in the degradation process. The holes left in the valance band oxidizes water to yield OH radicals which interact with organic pollutant to give less harmful reaction product. In case of  $\text{Bi}_2\text{WO}_6$  photocatalyst, major degradation species are  $\text{O}_2^-$  and photogenerated holes (depends on bonding of catalyst with the pollutant). The combined effect of photocatalytic and electrocatalytic oxidation processes influences degradation performance of  $\text{Bi}_2\text{WO}_6$  electrode. The chemical kinetics of the degradation reaction was studied by using pseudo-first-order kinetic law.

$$\ln\left(\frac{C}{C_0}\right) = -kt \quad (10)$$

Where,  $k$  is the kinetic rate constant of the reaction and  $t$  is the illumination time [41]. Fig. 8(b) illustrates kinetics of degradation reaction of RhB under solar radiation.

The  $\ln(C_t/C_0)$  shows straight line nature after plotting against time  $t$  which confirms photoelectrocatalytic degradation of RhB obeys first

order reaction kinetics. The slope of the line  $1.08 \times 10^{-4} \text{s}^{-1}$  gives constant  $k$ . It depends on the surface area of photoanode and intensity of the light source. For comparative study, other kinetic parameters were calculated by using following relations [40].

$$k' = kV \text{ (cm}^3\text{s}^{-1}\text{)} \quad (11)$$

$$k' = \frac{k'}{A} \text{ (cms}^{-1}\text{)} \quad (12)$$

$$k'' = \frac{kVF}{i} \text{ (M}^{-1}\text{)} \quad (13)$$

where,  $k'$ ,  $k''$  and  $k'''$  are rate constants,  $V$  is the total volume of organic pollutant under treatment,  $i_{\text{ph}}$  is total photocurrent,  $A$  and  $F$  are the area of photoelectrode and Faraday's constant ( $96,500 \text{ mol}^{-1}$ ), respectively. The constant  $k'''$  is a measure of oxidative degradation of organic species.

### 3.8. Stability of $\text{Bi}_2\text{WO}_6/\text{FTO}$ electrode

The stability and reusability of  $\text{Bi}_2\text{WO}_6$  photoelectrode were tested by carrying out PEC degradation of 250 ml RhB solution by  $\text{Bi}_2\text{WO}_6/\text{FTO}$  electrode at bias potential 0.7 V under solar light. The same degradation experiment was carried out three times with fresh RhB solution. After each degradation cycle, film was cleaned by ultrasonication in double distilled water. Fig. 9 indicates the nature of degradation efficiency of  $\text{Bi}_2\text{WO}_6$  photoelectrode against the number of cycles.  $\text{Bi}_2\text{WO}_6$  film possesses excellent photoelectrocatalytic stability as there is no apparent change in its performance after four consecutive PEC runs.

Table 4 indicates various kinetic parameters and efficiency of photoelectrocatalytic degradation of RhB. There are few reports on application of  $\text{Bi}_2\text{WO}_6$  film for photoelectrocatalytic waste water treatment. Table 4 represent degradation performance of  $\text{Bi}_2\text{WO}_6$  photoelectrode reported till date.

## 4. Conclusion

In summary,  $\text{Bi}_2\text{WO}_6$  photocatalyst immobilized on FTO substrate by spray pyrolysis technique can efficiently degrade RhB with the application of external bias potential under solar radiation. An effective separation of photogenerated charge carriers in photoelectrocatalytic degradation process was responsible for higher performance than photocatalytic process. The volume of spraying solution significantly affects crystallinity, morphology, photoelectrochemical and optical properties of  $\text{Bi}_2\text{WO}_6$  films. The optimized film showed higher crystallinity and photocurrent density. Photoelectrocatalytic degradation of RhB obeys pseudo first order kinetics and showed 94% degradation efficiency. This work would account for potential application of  $\text{Bi}_2\text{WO}_6$  films in wastewater treatment and photocatalytic water splitting.

### CRedit authorship contribution statement

**R.S. Pedanekar:** Conceptualization, Writing – original draft, Methodology, Investigation. **S.B. Madake:** Software, Visualization. **N.A. Narewadikar:** Visualization. **S.V. Mohite:** Data curation. **A.R. Patil:** Software. **S.M. Kumbhar:** Data curation. **K.Y. Rajpure:** Writing – review & editing, Supervision.

Table 4  
Degradation of organic pollutant by  $\text{Bi}_2\text{WO}_6$  photoelectrode so far.

Photoelectrode	Method	Pollutant	Light source	Pollutant Volume and concentration	Efficiency	Refs.
$\text{Bi}_2\text{WO}_6/\text{FTO}$	Solvothermal	Phenol	500 W Xe	15 ml (10 mg/L)	78%	[20]
$\text{Bi}_2\text{WO}_6/\text{ITO}$	Hydrothermal	RhB	500 W Xe	150 mL	87.2%	[42]
$\text{Bi}_2\text{WO}_6/\text{ITO}$	Hydrothermal	4-Chlorophenol (4-CP)	500 W Xe	100 mL	53%	[36]
$\text{Bi}_2\text{WO}_6/\text{FTO}$	Spray Pyrolysis	RhB	Sunlight	250 ml (30 mg/L)	94%	Present work

## CRediT authorship contribution statement

**R.S. Pedanekar:** Conceptualization, Writing – original draft, Methodology, Investigation. **S.B. Madake:** Software, Visualization. **N.A. Narewadikar:** Visualization. **S.V. Mohite:** Data curation. **A.R. Patil:** Software. **S.M. Kumbhar:** Data curation. **K.Y. Rajpure:** Writing – review & editing, Supervision.

## Declaration of Competing Interest

The authors declare that they have no known competing financial interests or personal relationships that could have appeared to influence the work reported in this paper.

## Acknowledgments

Author R. S. Pedanekar and N.A. Narewadikar are thankful to Chhatrapati Shahu Maharaj Research Training and Human Development Institute (SARTHI), Pune (India) for financial support through Chhatrapati Shahu Maharaj National Research Fellowship (CSMNRF). This work is partially supported by University Grant Commission (UGC) and Department of Science and Technology (DST), Government of India through providing facilities under DSA-SAP Phase-II and PURSE Phase-II program at the Department of Physics, Shivaji University, Kolhapur.

## References

- [1] B.T. Long, Inverse algorithm for Streeter–Phelps equation in water pollution control problem, *Math. Comput. Simul.* 171 (2020) 119–126, <https://doi.org/10.1016/j.matcom.2019.12.005>.
- [2] E. Boelee, G. Geerling, B. van der Zaan, A. Blauw, A.D. Vethaak, Water and health: from environmental pressures to integrated responses, *Acta Trop.* 193 (2019) 217–226, <https://doi.org/10.1016/j.actatropica.2019.03.011>.
- [3] A. Houas, H. Lachheb, M. Ksibi, E. Elaloui, C. Guillard, J.M. Herrmann, Photocatalytic degradation pathway of methylene blue in water, *Appl. Catal. B Environ.* 31 (2001) 145–157, [https://doi.org/10.1016/S0926-3373\(00\)00276-9](https://doi.org/10.1016/S0926-3373(00)00276-9).
- [4] R.D. Suryavanshi, K.Y. Rajpure, Spray deposited Fe<sub>2</sub>O<sub>3</sub> and stratified Fe<sub>2</sub>O<sub>3</sub>/ZnO novel photoelectrode for photoelectrocatalytic degradation of benzoic acid under solar light illumination, *J. Photochem. Photobiol. A Chem.* 357 (2018) 72–80, <https://doi.org/10.1016/j.jphotochem.2018.02.008>.
- [5] M.A. Mahadik, S.S. Shinde, K.Y. Rajpure, C.H. Bhosale, Photocatalytic oxidation of Rhodamine B with ferric oxide thin films under solar illumination, *Mater. Res. Bull.* 48 (2013) 4058–4065, <https://doi.org/10.1016/j.materresbull.2013.06.031>.
- [6] L. Finegold, J.L. Cude, Biological sciences: one and two-dimensional structure of alpha-helix and beta-sheet forms of poly(L-Alanine) shown by specific heat measurements at low temperatures (1.5–20K), *Nature* 238 (1972) 38–40, <https://doi.org/10.1038/238038a0>.
- [7] B.L.W. Zhang, Y.J. Wang, H.Y. Cheng, W.Q. Yao, Y.F. Zhu, Synthesis of porous Bi<sub>2</sub>WO<sub>6</sub> thin films as efficient visible-light-active photocatalysts, *Adv. Mater.* 21 (2009) 1286–1290, <https://doi.org/10.1002/adma.200801354>.
- [8] M. Mishra, D.M. Chun, α-Fe<sub>2</sub>O<sub>3</sub> as a photocatalytic material: a review, *Appl. Catal. A Gen.* 498 (2015) 126–141, <https://doi.org/10.1016/j.apcata.2015.03.023>.
- [9] R. Ameta, S. Benjamin, A. Ameta, S.C. Ameta, Photocatalytic degradation of organic pollutants: a review, *Mater. Sci. Forum.* 734 (2013) 247–272, <https://doi.org/10.4028/www.scientific.net/MSF.734.247>.
- [10] R. Shwetharani, H.R. Chandan, M. Sakar, G.R. Balakrishna, K.R. Reddy, A. V. Raghu, Photocatalytic semiconductor thin films for hydrogen production and environmental applications, *Int. J. Hydrogen Energy* 45 (2020) 18289–18308, <https://doi.org/10.1016/j.ijhydene.2019.03.149>.
- [11] X. Xu, Y. Ge, B. Li, F. Fan, F. Wang, Shape evolution of Eu-doped Bi<sub>2</sub>WO<sub>6</sub> and their photocatalytic properties, *Mater. Res. Bull.* 59 (2014) 329–336, <https://doi.org/10.1016/j.materresbull.2014.07.050>.
- [12] R.S. Pedanekar, S.K. Shaikh, K.Y. Rajpure, Thin film photocatalysis for environmental remediation: a status review, *Curr. Appl. Phys.* 20 (2020) 931–952, <https://doi.org/10.1016/j.cap.2020.04.006>.
- [13] M.B. Tahir, M. Sagir, M. Zubair, M. Rafique, I. Abbas, M. Shakil, I. Khan, S. Afshen, A. Hasan, A. Ahmed, WO<sub>3</sub> nanostructures-based photocatalyst approach towards degradation of RhB dye, *J. Inorg. Organomet. Polym. Mater.* 28 (2018) 1107–1113, <https://doi.org/10.1007/s10904-017-0771-x>.
- [14] C. Loka, K.S. Lee, Preparation and photocatalytic performance of silver nanocrystals loaded Cu<sub>2</sub>O-WO<sub>3</sub> composite thin films for visible light-active photocatalysis, *Mater. Res. Bull.* 137 (2021), 111192, <https://doi.org/10.1016/j.materresbull.2020.111192>.
- [15] H.A.I.T. Ahsaine, A. Taoufiq, M. Ezahri, J. Gavarri, Synthesis and Characterization of Bismuth Tungstate Bi<sub>2</sub>WO<sub>6</sub> and its Effect Towards the Degradation of Methylene Blue, 13th International Symposium on Nondestructive Characterization of Materials (NDCM-XIII), (2013).
- [16] S. Chaiwichian, B. Inceesungvorn, K. Wetchakun, S. Phanichphant, W. Kangwansupamonkon, N. Wetchakun, Highly efficient visible-light-induced photocatalytic activity of Bi<sub>2</sub>WO<sub>6</sub>/BiVO<sub>4</sub> heterojunction photocatalysts, *Mater. Res. Bull.* 54 (2014) 28–33, <https://doi.org/10.1016/j.materresbull.2014.03.012>.
- [17] C. Cheng, Z. Du, L. Tan, J. Lan, S. Jiang, R. Guo, L. Zhao, Preparation and visible-light photocatalytic activity of bismuth tungstate/lotus fiber composite membrane, *Mater. Lett.* 210 (2018) 16–19, <https://doi.org/10.1016/j.matlet.2017.08.114>.
- [18] B.Y. Alfaifi, A.A. Tahir, K.G.U. Wijayantha, Fabrication of Bi<sub>2</sub>WO<sub>6</sub> photoelectrodes with enhanced photoelectrochemical and photocatalytic performance, *Sol. Energy Mater. Sol. Cells* 195 (2019) 134–141, <https://doi.org/10.1016/j.solmat.2019.02.031>.
- [19] R.M. Silva, D.A. Batista Barbosa, C. de Jesus Silva Mendonça, J.R. de Oliveira Lima, F.C. Silva, E. Longo, A.P. Maciel, C.W. de Araujo Paschoal, M.A.P. Almeida, Morphological evolution and visible light-induced degradation of Rhodamine 6G by nanocrystalline bismuth tungstate prepared using a template-based approach, *J. Phys. Chem. Solids* 96–97 (2016) 83–91, <https://doi.org/10.1016/j.jpcs.2016.05.004>.
- [20] S. Sun, W. Wang, L. Zhang, Efficient contaminant removal by Bi<sub>2</sub>WO<sub>6</sub> films with nanoleaflike structures through a photoelectrocatalytic process, *J. Phys. Chem. C* 116 (2012) 19413–19418, <https://doi.org/10.1021/jp306332x>.
- [21] C. Chang, Y. Wei, W. Kuo, Free-standing CuS–ZnS decorated carbon nanotube films as immobilized photocatalysts for hydrogen production, *Int. J. Hydrogen Energy* 44 (2019) 30553–30562, <https://doi.org/10.1016/j.ijhydene.2018.04.229>.
- [22] X. Zhao, Y. Wu, W. Yao, Y. Zhu, Photoelectrochemical properties of thin Bi<sub>2</sub>WO<sub>6</sub> films, *Thin Solid Films* 515 (2007) 4753–4757, <https://doi.org/10.1016/j.tsf.2006.11.017>.
- [23] B.Y. Alfaifi, H. Bayahia, A.A. Tahir, Highly efficient nanostructured Bi<sub>2</sub>WO<sub>6</sub> thin film electrodes for photoelectrochemical and environment remediation, *Nanomaterials* 9 (2019), <https://doi.org/10.3390/nano9050755>.
- [24] S. Zhang, J. Shen, H. Fu, W. Dong, Z. Zheng, L. Shi, Bi<sub>2</sub>WO<sub>6</sub> photocatalytic films fabricated by layer-by-layer technique from Bi<sub>2</sub>WO<sub>6</sub> nanoplates and its spectral selectivity, *J. Solid State Chem.* 180 (2007) 1456–1463, <https://doi.org/10.1016/j.jssc.2007.02.013>.
- [25] Photocatalytic visible-light active bismuth tungstate coatings deposited by reactive magnetron sputtering, *Vacuum* 115 (2015) 66–69, <https://doi.org/10.1016/j.vacuum.2015.02.008>.
- [26] C. Sun, Y. Wang, Q. Su, Sol-gel synthesis of Bi<sub>2</sub>WO<sub>6</sub>/graphene thin films with enhanced photocatalytic performance for nitric monoxide oxidation under visible light irradiation, *Chem. Phys. Lett.* 702 (2018) 49–56, <https://doi.org/10.1016/j.cplett.2018.04.052>.
- [27] S. Sun, W. Wang, L. Zhang, J. Xu, Bi<sub>2</sub>WO<sub>6</sub>/SiO<sub>2</sub> photonic crystal film with high photocatalytic activity under visible light irradiation, *Appl. Catal. B Environ.* 125 (2012) 144–148, <https://doi.org/10.1016/j.apcatb.2012.05.039>.
- [28] V.V. Ganbavle, S.V. Mohite, G.L. Agawane, J.H. Kim, K.Y. Rajpure, Nitrogen dioxide sensing properties of sprayed tungsten oxide thin film sensor: effect of film thickness, *J. Colloid Interface Sci.* 451 (2015) 245–254, <https://doi.org/10.1016/j.jcis.2015.04.001>.
- [29] K.S. Knight, The crystal structure of russellite; a re-determination using neutron powder diffraction of synthetic Bi<sub>2</sub>WO<sub>6</sub>, *Mineral. Mag.* 56 (1992) 399–409, <https://doi.org/10.1180/minmag.1992.056.384.13>.
- [30] A. Phuruangrat, P. Dumrongrojthanath, N. Ekthammathat, S. Thongtem, T. Thongtem, Light-Driven Photocatalytic Properties of Bi<sub>2</sub>WO<sub>6</sub> Nanoplates, *J. Nanomater.* (2014), <https://doi.org/10.1155/2014/138561>.
- [31] M. Maczka, J. Hanuza, W. Paraguassu, A.G.S. Filho, P.T.C. Freire, J.M. Filho, Phonons in ferroelectric Bi<sub>2</sub>WO<sub>6</sub>: Raman and infrared spectra and lattice dynamics, *Appl. Phys. Lett.* 92 (2008) 10–13, <https://doi.org/10.1063/1.2896312>.
- [32] H. Fu, L. Zhang, W. Yao, Y. Zhu, Photocatalytic properties of nanosized Bi<sub>2</sub>WO<sub>6</sub> catalysts synthesized via a hydrothermal process, *Appl. Catal. B Environ.* 66 (2006) 100–110, <https://doi.org/10.1016/j.apcatb.2006.02.022>.
- [33] Y.M. Hunge, A.A. Yadav, M.A. Mahadik, V.L. Mathe, C.H. Bhosale, A highly efficient visible-light responsive sprayed WO<sub>3</sub>/FTO photoanode for photoelectrocatalytic degradation of brilliant blue, *J. Taiwan Inst. Chem. Eng.* 85 (2018) 273–281, <https://doi.org/10.1016/j.jtice.2018.01.048>.
- [34] Y.M. Hunge, M.A. Mahadik, S.S. Kumbhar, V.S. Mohite, K.Y. Rajpure, N. G. Deshpande, A.V. Moholkar, C.H. Bhosale, Visible light catalysis of methyl orange using nanostructured WO<sub>3</sub> thin films, *Ceram. Int.* 42 (2016) 789–798, <https://doi.org/10.1016/j.ceramint.2015.08.178>.
- [35] J. Li, X. Zhang, Z. Ai, F. Jia, L. Zhang, J. Lin, Efficient visible light degradation of Rhodamine B by a photo-electrochemical process based on a Bi<sub>2</sub>WO<sub>6</sub> nanoplate film electrode, *J. Phys. Chem. C* 111 (2007) 6832–6836, <https://doi.org/10.1021/jp070694z>.
- [36] X. Zhao, T. Xu, W. Yao, C. Zhang, Y. Zhu, Photoelectrocatalytic degradation of 4-chlorophenol at Bi<sub>2</sub>WO<sub>6</sub> nanoflake film electrode under visible light irradiation, *Appl. Catal. B Environ.* 72 (2007) 92–97, <https://doi.org/10.1016/j.apcatb.2006.10.006>.
- [37] R. Radha, A. Srinivasan, P. Manimuthu, S. Balakumar, Tailored sunlight driven nano-photocatalyst: bismuth iron tungstate (BiFeWO<sub>6</sub>), *J. Mater. Chem. C* 3 (2015) 10285–10292, <https://doi.org/10.1039/c5ra02284j>.
- [38] F. Ren, J. Zhang, Y. Wang, Enhanced photocatalytic activities of Bi<sub>2</sub>WO<sub>6</sub> by introducing Zn to replace Bi lattice sites: a first-principles study, *RSC Adv.* 5 (2015) 29058–29065, <https://doi.org/10.1039/c5ra02735g>.
- [39] S. Jonjana, A. Phuruangrat, S. Thongtem, T. Thongtem, Synthesis, characterization and photocatalysis of heterostructure AgBr/Bi<sub>2</sub>WO<sub>6</sub> nanocomposites, *Mater. Lett.* 216 (2018) 92–96, <https://doi.org/10.1016/j.matlet.2018.01.005>.
- [40] S.V. Mohite, V.V. Ganbavle, V.V. Patil, K.Y. Rajpure, Photoelectrocatalytic degradation of benzoic acid using immobilized tungsten trioxide photocatalyst,

- Mater. Chem. Phys. 183 (2016) 439–446, <https://doi.org/10.1016/j.matchemphys.2016.08.051>.
- [41] B.Y. Alfaifi, H. Bayahia, A.A. Tahir, Highly efficient nanostructured Bi<sub>2</sub>WO<sub>6</sub> thin film electrodes for photoelectrochemical and environment remediation, Nanomaterials 9 (2019). <https://doi.org/10.3390/nano9050755>.
- [42] J. Li, X. Zhang, Z. Ai, F. Jia, L. Zhang, J. Lin, Efficient visible light degradation of Rhodamine B by a photo-electrochemical process based on a Bi<sub>2</sub>WO<sub>6</sub> nanoplate film electrode 111 (2007) 6832–6836, <https://doi.org/10.1021/jp070694z>.